molecular pharmaceutics

pubs.acs.org/molecularpharmaceutics

Article

Monoclonal Antibody Delivery Using 3D Printed Biobased Hollow μNe3dle Arrays for the Treatment of Osteoporosis

Published as part of the Molecular Pharmaceutics virtual special issue "Recent Developments in Transdermal Microneedle Drug Delivery".

Md Jasim Uddin, Sophia Nikoletta Economidou, Léa Guiraud, Mohsin Kazi, Fars K. Alanazi, and Dennis Douroumis*

Cite This: *Mol. Pharmaceutics* 2024, 21, 4465−4475

Read Online

ACCESS | Metrics & More | Article Recommendations

ABSTRACT: Transdermal microneedles have demonstrated promising potential as an alternative to typical drug administration routes for the treatment of various diseases. As microneedles offer lower administration burden with enhanced patient adherence and reduced ecological footprint, there is a need for further exploitation of microneedle devices. One of the main objectives of this work was to initially develop an innovative biobased photocurable resin with high biobased carbon content comprising isobornyl acrylate (IBA) and pentaerythritol tetraacrylate blends (50:50 wt/wt). The optimization of the printing and curing process resulted in μNe3dle arrays with durable mechanical properties and piercing capacity. Another objective of the work was to employ the 3D printed hollow μNe3dles for the treatment of osteoporosis in vivo. The 3D printed μNe3dle arrays were used to administer denosumab (Dmab), a monoclonal antibody, to osteoporotic mice, and the serum concentrations of critical bone minerals were monitored for six months to assess recovery. It was found that the Dmab administered by the 3D printed μNe3dles showed fast in vitro rates and induced an enhanced therapeutic effect in restoring bone-related minerals compared to subcutaneous injections. The findings of this study introduce a novel green approach with a low ecological footprint for 3D printing of biobased μNe3dles, which can be tailored to improve clinical outcomes and patient compliance for chronic diseases.

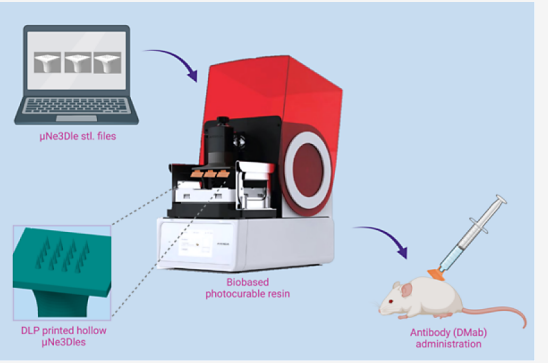

KEYWORDS: *3D printing, digital, light Processing, microneedles, monoclonal Antibody, osteoporosis*

1. INTRODUCTION

Osteoporosis is a common chronic bone disease associated with aging that increases bone fragility and renders bones prone to fracture, with patient population estimates up to 200 million worldwide.[1] Denosumab (Dmab), a human recombinant monoclonal antibody, has been approved for administration to osteoporotic patients who are at a high risk of fracture due to its ability to increase bone mineral density.[2] Dmab is typically administered via subcutaneous injection in six-month intervals. Alternative administration routes have not yet been explored.

The transdermal drug delivery route has received significant attention in previous years, especially with the introduction of the microneedle concept, as a means to overcome the high impermeability of the skin tissue. Microneedles are miniature devices that achieve efficient disruption of the skin barrier to directly introduce drugs to the dermal microcirculation.[3] Their dimensions entail minimal damage of the skin nerves, and thus pain during drug administration is minimized.[4] Microneedles have been extensively tested for their ability to convey various therapeutic and immunization substances including macromolecules, hydrophilic drugs, and vaccines.

In the field of osteoporosis treatment, research on the applicability of microneedles has been limited. Katsumi et al. proposed a patch of dissolvable microneedles that featured a cargo of alendronate exclusively in the tip area. In vivo studies on postmenopausal rats showed that the transdermal microneedle-mediated route was more effective at treating osteoporosis than oral administration.[5] Along the same lines, Zosano Pharma developed a coated microneedle patch loaded with parathyroid hormone (I-34) and conducted phase I and phase II clinical studies. They found that the patch achieved rapid hormone

Received: April 6, 2024
Revised: July 29, 2024
Accepted: July 29, 2024
Published: August 7, 2024

delivery and an increase in spinal bone mineral density. Interestingly, the patch was also found to induce an early increase of bone mineral density at the hip area, which was not observed for the injection-treated subjects.[6] Furthermore, microneedle patches have been systematically studied for the in vivo administration of antibodies, proteins, and peptides. Furthermore, the applications of microneedle patches for transdermal delivery offer a wide versatility for the development of novel drug delivery systems such as vaccines and DNA-non-viral therapy.[7−10] In such a study, Shakya et al. (2020)[11] used microneedles for the delivery of cyclic diguanylate monophosphate and cyclic diadenylate monophosphate for skin allergen-specific immunotherapy.[12] The results showed higher levels of Th1 cytokines and much better activation compared to subcutaneous injections. The same group demonstrated that microneedle patches can be applied for the administration of allergens to overcome issues of subcutaneous allergen-specific immunotherapy.[13] These findings indicate that microneedles may have untapped potential to improve the therapeutic effects of existing treatments.

Microneedles are routinely manufactured mainly through micromolding, micromachining, and etching, which often require sophisticated equipment and can be noneconomical for small product numbers.[14−19] 3D printing or additive manufacturing has emerged as a simple, effective, and reliable microneedle manufacturing alternative to traditional methods. Several studies have been conducted on the manufacturability of solid microneedles via stereolithography (SLA), a photopolymerization-based 3D printing technology.[20−22] The swift nature of the technology has allowed the tailoring of geometrical parameters to achieve different delivery profiles, aligned with individual requirements in a cost-effective and time-efficient manner.[23] Recently, our group presented a strategy for obtaining hollow μNe3dle patches fabricated via SLA. The patches were developed as part of a combinatorial device composed of the 3D printed hollow μNe3dles and a microelectromechanical system (MEMS).[24] A complex patch featuring hollow μNe3dles and an internal reservoir, with excellent skin piercing capability and mechanical strength, was fabricated using SLA. The versatile geometry of the patch prompted the attempt to investigate its independent use in the clinical setting as a readily available alternative to typical needles fitted on standard syringes.

Currently, photopolymer resins comprised fossil-based materials, which are expensive, and have large carbon footprint, which limits the applicability of 3D printing for medical devices.[25] Hence, there is an enormous need to develop sustainable alternatives for environmentally friendly and cost-effective resins that promote a circular economy. There are several studies that investigate the development of biodegradable or recyclable biobased resins using a range of renewable resources such as vegetable oils, lignin, cellulose, poly(propylene) fumarate, and e-polycarpolactone.[26,27]

Here, we introduce the development of a low cost, biobased resin comprising IBA and PETA blends with high biobased carbon content for the fabrication of μNe3Dle arrays with high precision accuracy and mechanical strength. Furthermore, we present for the first time the development and in vivo efficacy evaluation of a 3D printed hollow μNe3dle-syringe drug delivery system for the treatment of osteoporosis.[28,29] Osteoporotic animal models were developed and subjected to a 6-month study that investigated the therapeutic impact of Dmab, administered by hollow μNe3dles. The recovery of bone-related minerals was monitored to assess the efficacy of the system and enable its comparison with the traditional route via subcutaneous injection. The present study aims at demonstrating the multifunctionality of 3D printed hollow μNe3dles as a potential tool for the transdermal delivery of a wide range of therapeutic substances.

2. MATERIALS AND METHODS

2.1. Materials. Denosumab (Dmab), a human monoclonal antibody (Denosis 60; 147 kDa), was purchased from Incepta Pharmaceuticals Limited (Dhaka, Bangladesh). The product contained 1 mL of sterile solution of 60 mg Dmab. Pentaerythritol tetraacrylate (PETA), isobornyl acrylate (IBA), and diphenyl (2,4,6 trimethyl benzoyl) phosphine oxide (Irgacure TPO) were purchased from Sigma-Aldrich (Gillingham, UK).

2.2. Resin Synthesis. A photocurable resin was synthesized using IBA-PETA (90:10 wt/wt ratio) and TPO (1%) as the photoinitiator. PETA was added to the IBA resin and stirred under the dark for 8 h followed by the addition of TPO and stirred for another 1 h.

2.3. Development of the μNe3dle -Syringe Drug Delivery System. Hollow μNe3dle patches were designed and 3D etched using a MAX X27 DLP (Asiga, Erfurt, Germany). The development of the complex hollow microneedle patches featuring 4 μNe3dles each and an internal reservoir was conducted in accordance with the processes presented elsewhere.[30] The μNe3dle height was 1000 μm with a tip of 100 μm. The design, additive manufacturing, and postprinting treatment processes were followed precisely. The 3D printed patches were originally designed to be tightly fitting components with standard syringes. Their assembly was conducted through tight fit to avoid liquid losses.

2.4. Mechanical Testing of 3D Printed Hollow μNe3dles. In order to assess the impact of curing parameters, including temperature and duration, on the mechanical characteristics of the synthetic resin, a number of cylinders were printed and then exposed to varying curing conditions. The predefined chamber periods of 30, 45, and 60 min were associated with the preset curing temperatures of 40, 50, and 60 °C. For each set of temperature and time, three specimens were examined.

The compression tests were conducted using a Tinius Olsen H25KS mechanical testing equipment (Tinius Olsen, Surrey, UK) with a 25 kN load cell, in accordance with the ASTM D695 Standard Test Method for Compressive Properties of Rigid Plastic. Each printed cylinder was placed between two flat test plates, and at a constant speed of 1.5 mm/min, a vertical force was applied along its longitudinal axis. The Horizon program (Paris, France) recorded and presented the results generated for each sample. True stress and true strain values were determined by analyzing the position and employed force values. The compressive modulus, yield strength, and ultimate strength of every specimen were subsequently determined through the 0.5% offset curve approach.

2.5. Preparation of Skin Samples for the Piercing Test. The freshly obtained full-thickness porcine skin from a local slaughterhouse (Forge Farm Ltd., Kent, UK) was selected for the piercing test as it represents the similar biological system of higher animals (e.g., human skin). The collected skin samples were preserved in the refrigerator at 4 °C in previously prepared PBS pH 7.4 until the excision procedure was conducted. An electric razor (Panasonic, USA) was used to remove any excess hair on the skin before the piercing studies. Initially, the fatty

https://doi.org/10.1021/acs.molpharmaceut.4c00379
Mol. Pharmaceutics 2024, 21, 4465−4475

Table 1. Treatment Protocol for Denosumab Delivery

day	stage	treatment strategy
−7 days prior ovariectomy	animal model selection and isolation	transfer mice to study isolator
0	induction of osteoporosis	surgical procedures of ovariectomy
1−27	observation	measurement of weight
28	confirmation of osteoporosis induction and Dmab therapy using hollow μNe3dles	after treatment, blood samples were collected from the jugular vein and the plasma concentrations of Dmab and bone related minerals were measuredthe study was conducted for 6 months uninterruptedly.

layer of porcine skin was removed followed by the excision of skin (1 mm in length) using a dermatome (Padgett Dermatome, Integra LifeSciences Corporation, Princeton, NJ, USA). The skin samples were then cut into the square shapes and hydration was maintained by storing in a Petri dishes containing buffer saline of pH 7.4, which were further transferred to the texture analyzer for the piercing test, which was mentioned in our previous work.[31]

2.6. Piercing Tests of Hollow μNe3dles. The penetration capacity of 3D printed hollow MNs was studied using a TA. A HD plus Texture Analyzer (Stable Micro Systems, Surrey, UK) with a 5 kg load cell was used. The compression forces were set in consideration to MN length, skin physiology, and removal capacity of 3D MN. Precompression and postcompression forces were applied as 1.00 mm/s, while test compression was applied as 0.1 mm/sec, respectively. The dermatomed-full thickness skin was placed onto the Petri dishes, while 3D hollow MN fixed was fixed onto the probe using a double-sided adhesive tape (3M, USA). The piercing tests were carried out six times for repeatability and reproducibility. The point of needle insertion was determined using two parameters: continuous force and displacement measurements.

2.7. Preparation of Mice Skin Samples for In Vitro Studies. Female Swiss albino mice were euthanized to obtain dorsal skin samples for the in vitro release studies. After euthanasia, the mice were fixed on the working bench with their abdominal areas exposed. Fresh full-thickness abdominal skin was excised from the cadavers using a scalpel. The superficial skin hair was removed using an electric razor. The thickness of the skin samples was measured with a digital caliper and was found to be 1.0 ± 0.2 mm. The skin samples were placed in phosphate-buffered saline (PBS) before experimentation.

2.8. In Vitro Release Studies Through the Dorsal Mouse Skin. The ability of the 3D printed hollow μNe3dles to deliver dmabsumab through the dorsal skin of Swiss albino female mice was examined by using Franz diffusion cells. Freshly excised dorsal skin samples were used throughout the experiment. The μNe3dle syringe system was used to pierce the skin and deliver 60 mg/mL of dmabsumab to the skin sample. The release of the drug was monitored by collecting aliquots from the receptor compartment of the Franz diffusion cells at the intervals of 10, 20, 30, 40, 50, and 60 min. The aliquots were analyzed by using an ELISA Assay Kit, Human, High Sensitivity (Eagle Biosciences, NH, USA).

2.9. Selection of Animals for In Vivo Clinical Studies. Swiss albino female mice (6−7 weeks; weighing 150−160 g) were purchased from the Animal Resources Facilities, International Centre for Diarrheal Disease Research, Bangladesh (icddr,b, Dhaka, Bangladesh) in good health. All animal experiments were conducted in accordance with Southern University Bangladesh principles. Procedures for the protection of Vertebrate Animals for Experimental and Other Scientific Purposes were applied, with implementation of the 3Rs principle (replacement, reduction, and refinement). The protocols for animal experimentation throughout this study were approved by the Animal Experimentation Committee (reference no. 0005/20, Department of Pharmacy, Southern University Bangladesh).

2.10. Development of an Osteoporotic Animal Model. The mice were subjected to ovariectomy to develop an osteoporotic animal model. Seven days prior to surgery, the animals were selected and isolated in separate cages. At the day of the surgery, the mice were anesthetized by isoflurane (5%) through the inhalation route. The surgery (dorsal approach) was carried out only after the attainment of anesthesia. The vaporization did not exceed 60 min in duration to avoid any respiration ceasing and possible death. The ovaries were removed according to the protocol described by Souza et al.[32] The ovarian capsules including the ovarian fat pad and part of the oviduct were removed to ensure the induction of osteoporosis. During the employed dorsal approach, care was taken not to remove the uterine horn. The surgery lasted 30−45 min including a recovery time of about 15 min. After 1 day, the surgical site was examined, and no ovarian tissue was detected during autopsy (data not provided). The animals were monitored and weighed daily for 27 days.

2.11. In Vivo Treatment of Osteoporosis with 3D Printed Hollow μNe3dles. The ability of 3D printed hollow μNe3dles to deliver dmabsumab to mice for the treatment of osteoporosis was explored. Prior to the animal study, osteoporotic female mice were given free access to solid bottom high cages (Anima Lab, Pozna, Poland) with controlled diet for 24 h. The animals were anesthetized under pentobarbital anesthesia (40 mg/kg as pentobarbital sodium salt) and shaved on the area of μNe3dle application using an electric razor (Panasonic, USA).

The animals were divided into 3 groups (n = 6 each):

i Untreated (negative control), received no treatment;

ii SC (positive control), received 0.14 mg/animal via subcutaneous injection;

iii 3DMN, received 0.14 mg/animal via the hollow μNe3dle/syringe system.

The animals treated with the device were held gently while the MN array was applied on the shaved dorsal area using manual finger pressure to reassure insertion. The above-mentioned volume of dmabsumab was delivered, in the form of a bolus dose, to imitate the typical subcutaneous injection treatment regime and allow comparison thereof. After administration, the system was detached instantly.

At predetermined intervals (0−6 h) after the dmabsumab administration and while the animals were placed under pentobarbital anesthesia (40 mg/kg as pentobarbital sodium salt), 0.3 mL blood samples were collected from the jugular vein and stored in tubes. The collected blood was then centrifuged for 15 min at 4000 rpm to acquire plasma. The plasma concentrations of denosumab were determined using a

https://doi.org/10.1021/acs.molpharmaceut.4c00379
Mol. Pharmaceutics 2024, 21, 4465−4475

Denosumab ELISA Assay Kit, Human, High Sensitivity (Eagle Biosciences, NH, USA). The treatment strategy is described in Table 1.

During experimentation, microscopic images of the hollow μNe3dles were captured through a computer-controlled compound microscope (Microscope LLC, Roanoke, VA, USA). An Optical Coherence Tomography (OCT) system (Carl Zeiss India Pvt. Limited, India) was used to monitor the penetration of the hollow μNe3dles into the skin (2 mm in depth). False color representation was used to identify the μNe3dle shafts, the stratum corneum, the epidermis, and the dermis.

2.12. Determination of Bone-Related Minerals. The changes of bone-related minerals (serum iron, copper, magnesium, and zinc) were investigated using specified analytical techniques. Serum iron was studied through the nitroso-2-nitroso-5-[N-n-propyl-N-(3-sulfopropyl) amino] phenol method, copper through the colorimetric method, magnesium by the xylidyl blue method, and zinc by atomic absorption spectroscopy. Mineral measurements and respective analyses were conducted at 1−6 months.

2.13. Statistical Analysis. The results are expressed as the mean ± standard errors. For the in vitro and in vivo studies, samples were considered as statistically significant at $p < 0.05$ (SPSS statistics, IBM Inc., USA). The secondary data generated from the in vivo studies were processed, and descriptive analysis including the calculation of means, variances, and standard deviations was done for each data set. Statistical tests such as the t test (paired) and ANOVA were carried out to test the significance of each data set. The confidence interval was set to 95%, and the p value was calculated. For $p < 0.05$, the null hypothesis (no statistically significant difference between data sets) is rejected and the alternate hypothesis is accepted.

3. RESULTS AND DISCUSSION

3.1. Synthesis and 3D Printing of the Hollow μNe3dle-Syringe Drug Delivery System. 3D printing has revolutionized the manufacturing of μNe3dle arrays and the transdermal delivery of drug substances over the last five years.[22,23] It offers particular advantages such as high-level geometric accuracy during the array fabrication and thus allows the fabrication of a variety of complex designs with different lengths, heights, and aspect ratios. Our group was the first to introduce stereolithography and later digital light processing for the customization of μNe3dle arrays by using a standard Dental SG resin (Formlabs) due to its excellent biocompatibility and mechanical properties. However, one of the drawbacks of 3D printing is the lack of resins, which are cost-efficient and biocompatible while presenting high printing accuracy and mechanical strength.[33]

The first part of this study involved the development of a resin formulation comprising biobased acrylate photopolymers. Hence, IBA, a monomer derived from pine resin with 75% of its carbons accounting as biobased (Figure 1), was used as formulation component.[34] Similarly, PETA, another tetrafunctional acrylate monomer with 10% biobased carbon, was selected as a second component of the developed photocurable resin. By using eq 1, the monomer combination resulted in a biobased carbon content (BC) of 64%.[35]

$$\mathrm{BC} = \frac{C_{\text{biobased}}}{C_{\text{biobased}} + C_{\text{petro-based}}} \times 100$$

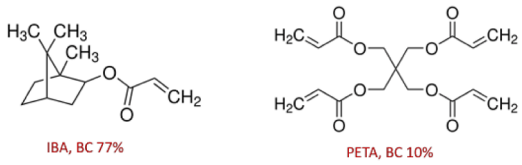

Figure 1. Structural formula and BC content of biobased acrylate monomers.

The biobased features of developed resins for the fabrication of μNe3dles can be further improved by investigating compositions with a higher BC percentage. Furthermore, both IBA and PETA are known biocompatible materials.[36] Nevertheless, the use of such innovative materials with lower ecological footprint will help to introduce greener manufacturing technologies for achieving a CO_2 neutral balance and eliminate waste in landfills.

Prior to printing of μNe3dle arrays, the postprinting curing conditions were further investigated to evaluate the effect on the mechanical properties of the biobased resins. Preliminary data demonstrated that by increasing the content of PETA, the mechanical properties of printed cylinders were significantly improved. These findings were in a good agreement with published work on the development of biocomposites.[37] The curing settings such as temperature and duration have been found to impact the Young's modulus and the ultimate strength due to their effect on the cross-linking density.

As shown in Figure 2, the printed cylinder specimens were subjected to different temperatures (40−60 °C) and exposure times (30−60 min). Based on the experimental findings, the optimal curing settings were identified at 40 °C for 30 min. The selection was related to highest values obtained for Young's modulus, yield strength, and breaking point at the faster curing time and lower temperature. It is obvious that both temperature and exposure time influence the obtained mechanical properties, which are directly related to the resin cross-linking. The comparison with previous results when a dental resin was used showed significant reduction on the curing time. In accordance with the manufacturing strategy presented elsewhere,[30] complex μNe3dle patches were 3D printed. The patches featured 4 cone-shaped μNe3dles each, in a symmetric 2 × 2 configuration. The hollow shafts were designed on a flat substrate and communicated by their bores with an internal reservoir at the bottom of the substrate.

The reservoir was connected to a cylindrical opening at the bottom of the patch that was designed to fit tightly on standard syringes (Figure 3a). After manufacturing, the patches were sterilized in an autoclave. Fracture and mechanical safety analyses were conducted in accordance with previous studies,[30] rendering the system mechanically safe for in vivo application (data not shown). The final assembly of the drug delivery system was carried out by simply fitting the patch to a syringe (Figure 3d).

3.2. Piercing Tests. The piercing forces were monitored and recorded during the piercing tests in the full thickness skin. Comparative studies were performed with 3D printed solid MN of similar dimensions. The experimental findings (Figure 4) were similar to our previous findings.[22−24,31,38]

All MNs showed similar piercing capacity with insertion forces of 35.9 ± 3.3 mN force/3D printed hollow MN and 36.9 ± 4.9 mN force/3D printed solid MN, respectively. At the commencement of the experiment, the slopes of the curves of 3D printed solid MN and hollow MN were constant. It was due

https://doi.org/10.1021/acs.molpharmaceut.4c00379
Mol. Pharmaceutics 2024, 21, 4465−4475

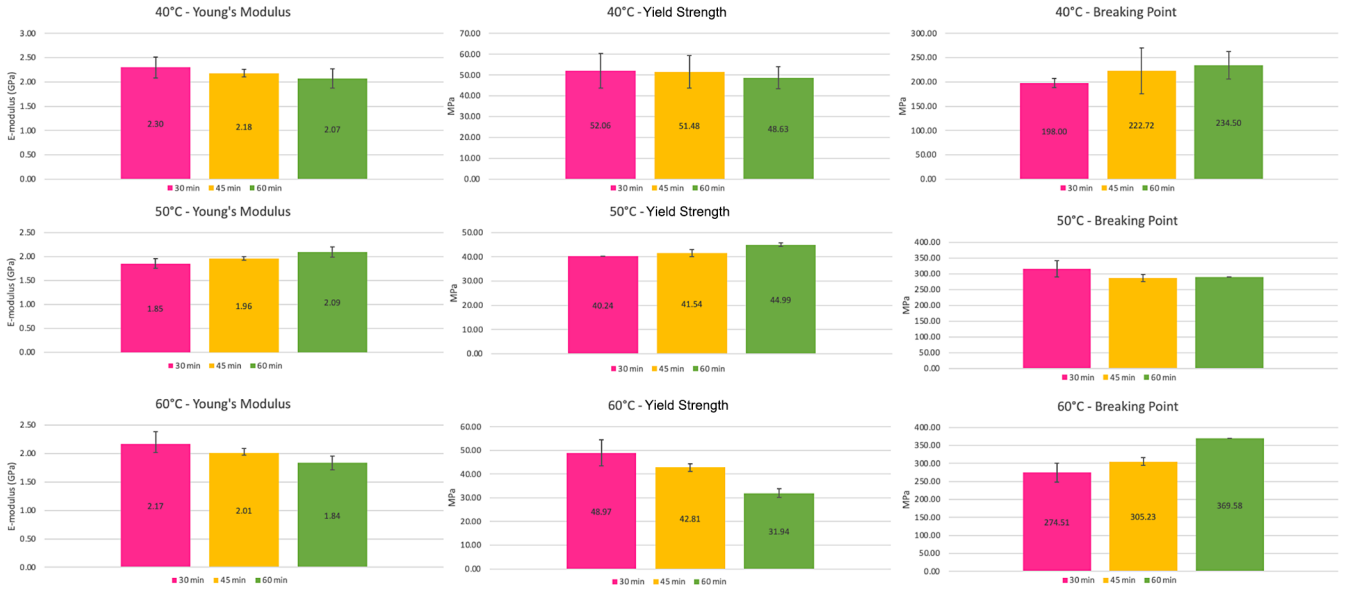

Figure 2. Optimization of the IBA/PETA (90:10 wt/wt) resin postprinting process using 3D printed cylinders under different curing settings of 40, 50, and 60 °C for 30, 45, and 60 min, in relation to their mechanical properties. The graphs illustrate the evaluation of Young's modulus, yield strength, and breaking point.

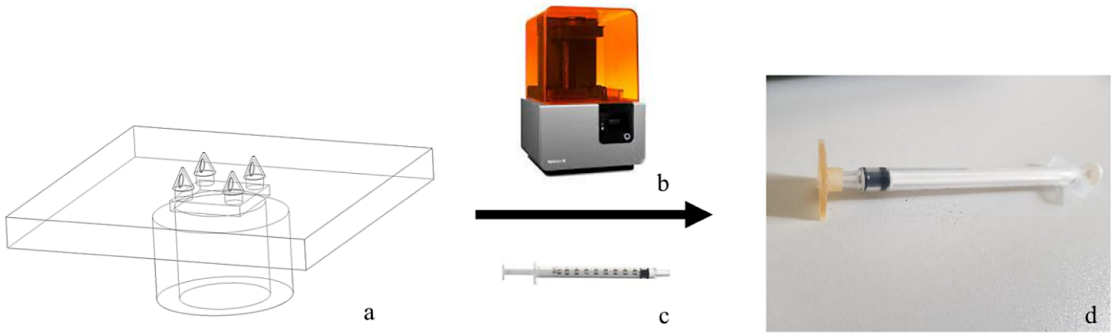

Figure 3. Development of the hollow μNe3dle/syringe system. (a) A virtual model of patch featuring 4 cone-shaped hollow μNe3dles and their bores, an internal reservoir, and the bottom opening for fluid provision; (b) a SLA 3D printer; (c) a standard syringe; and (d) an assembled μNe3dle-syringe drug delivery system.

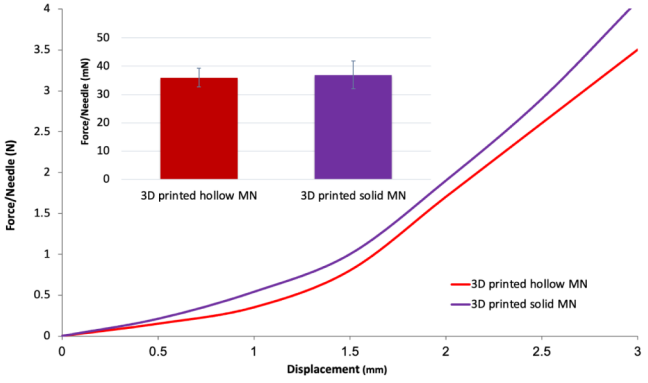

Figure 4. Piercing tests in porcine skin; force/needle vs displacement data; and insertion force/needle for 3D printed-hollow and 3D printed-solid MN (inset).

to the elastic deformation of the full thickness skin before piercing. Similar findings were reported elsewhere[30] in accordance with the respective literature that 3D printed hollow MN will cause minimal or no pain. It will also be beneficial in terms of patient compliance since it does not involve an application or trained health care practitioners.

3.3. In vitro Release Studies. Prior to the animal studies, the in vitro release of Dmab delivered by the hollow μNe3dles to mouse skin was investigated using Franz diffusion cells. The surgical procedure for collecting freshly excised dorsal skin is shown in Figure 5a–d. Dorsal skin was selected due to its uniform distribution of skin layers. The use of abdominal skin was avoided on the grounds of the latter being composed of thick layers of adipose tissue, which might interrupt the passage of high molecular weight drugs to the bloodstream. The parameters of Franz diffusion cells were discussed in previous studies.[24,39] A release profile was constructed over a time period of 60 min. The % Dmab release was recorded at 10 min intervals, meaning that six readings were recorded in one hour. As seen in Figure 2f, approximately 90% of the total amount delivered was detected in the receptor compartment in 1 h.

The prolonged release of Dmab was attributed to its larger molecular weight as well as to depot formation within the skin tissue, which acts as a drug reservoir underneath the skin and releases its content slowly by passive diffusion. Data and respective statistical analyses were conducted. For the

https://doi.org/10.1021/acs.molpharmaceut.4c00379
Mol. Pharmaceutics 2024, 21, 4465−4475

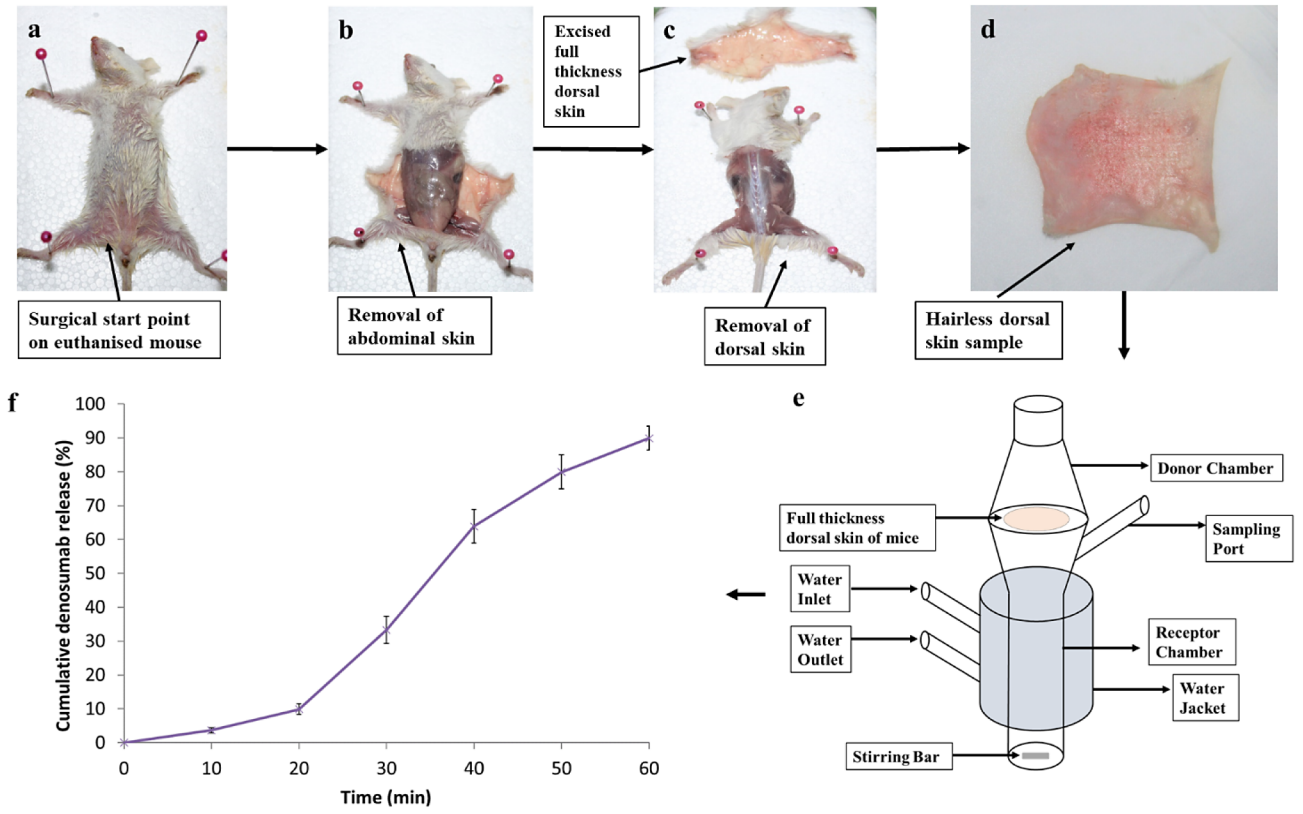

Figure 5. In vitro Dmab release studies using full thickness mouse skin. (a) Surgical start points on euthanized mice, (b) removal of abdominal skin, (c) removal of dorsal skin and the excision of a full thickness dorsal skin, (d) selection of hairless dorsal skin for diffusion studies, (e) in vitro release studies through skin using Franz diffusion cells, and (f) cumulative Dmab release at 0−60 min.

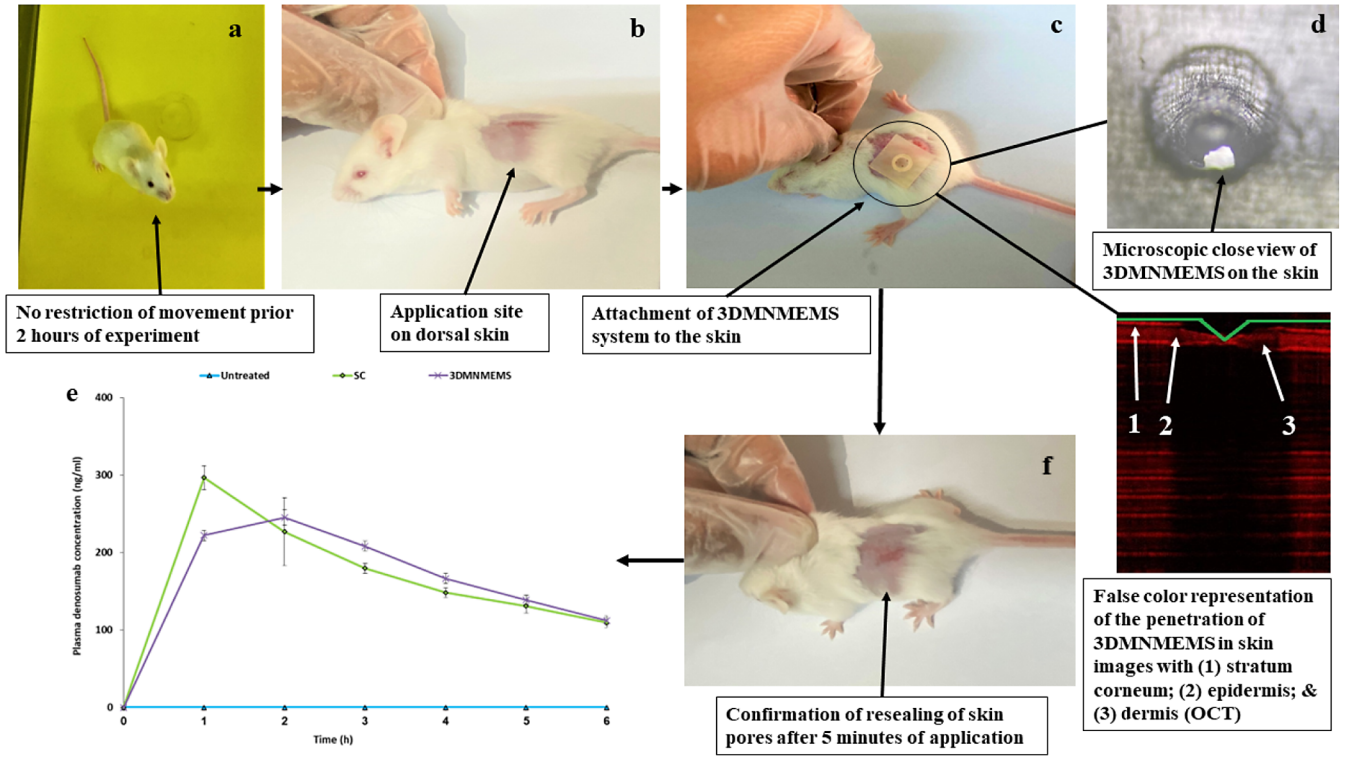

Figure 6. In vivo animal studies of Dmab administration to an osteoporotic mouse model using 3D printed hollow μNe3dles. (a) Unrestricted animal movement 2 h before the experiment, (b) shaved application site on dorsal skin, (c) application of the 3D printed μNe3dle patch and Dmab administration, (d) microscopic close view of the μNe3dle on the skin, (e) OCT image of the penetration μNe3dle penetration through the skin layers, (f) confirmation of skin pore resealing 5 min after application, and (e) monitoring of plasma Dmab concentration for 6 h after therapy.

https://doi.org/10.1021/acs.molpharmaceut.4c00379
Mol. Pharmaceutics 2024, 21, 4465−4475

cumulative release data, statistical tests such as Pearson correlation and linear regression modeling were performed.

The Pearson correlation test was carried out to investigate the relationship between the two continuous quantitative variables, with time being the independent variable and cumulative Dmab release being the dependent variable. The Pearson correlation coefficient (r), which determines the strength and direction of the relationship between the two variables, was calculated. The range of the coefficient is from −1 (strong negative relationship) to +1 (strong positive relationship). The obtained value of r was 0.975, which is very close to +1. This indicates a very strong positive correlation between the time and cumulative Dmab release. As time increases, the % Dmab release also increases almost linearly at a very similar rate. The p value obtained from the Pearson correlation analysis is 0.000194, which is less than the threshold of 0.05. Thus, the null hypothesis (which states that there is no significant difference between time and % Dmab release) is rejected, and the alternate hypothesis (there is a significant difference between the time and % Dmab release) is accepted. Thus, the test accounts for the significance of the data set.

Linear regression analysis was applied to determine the effect of the increase in the time variable on the % release of Dmab. The linearity of the data set was determined by the value of R^2, which was 0.975. This means that the higher proportion of variation in the dependent variable (% release) is attributed to the independent variable (time). The high value of 0.975 indicates that the data set fits very closely with the linear regression model. The p value obtained from this test was also 1.94×10^{-4}, which means that the data set is statistically significant.

3.4. Preclinical Investigation Using Animal Model In Vivo. Microneedle patches have been introduced for the administration of biopharmaceutics including a wide range of proteins, peptides, and antibodies offering enhanced therapeutic efficacy in comparison to conventional administration approaches such as intramascular or subcutaneous injections.[41,42] Several studies have shown that administration of such molecules does not rigger immunogenic effects while enhancing the bioavailability.[8,43] To our knowledge, this is the first study to date that puts forward the use of μNe3dles for the transdermal delivery of Dmab with the aim to treat osteoporosis in vivo. The therapeutic performance of Dmab delivered by 3D printed hollow μNe3dles was investigated on an osteoporotic animal model under the approved protocol discussed in the experimental section. The postmenopausal osteoporotic mouse model was created by performing ovariectomy on female Swiss albino mice. Four weeks after ovariectomy, the osteoporotic mice were separated into three groups: untreated (negative control), subcutaneously (SC) injected (positive control), and treated with the 3D printed hollow μNe3dles (3DMN). The amount of drug administered to the SC and 3DMN groups was identical. The in vivo experimentation process is illustrated in Figure 6. The 3D printed microneedle patches were inserted in the shaved dorsal skin using thumb pressure, and the drug containing syringe was used to administer the drug (Figure 6c). OCT images of the μNe3dles embedded into the skin illustrate the successful penetration of the device. The μNe3dles are shown to surpass the epidermis and reach the dermis, which is essential for fast drug absorption by the skin capillary bed (Figure 6).

A single dose of Dmab was administered in order to avoid overdose in mice. A well-documented issue related to Dmab administration is its association with adverse dermatological reactions.[40] A first measure taken to tackle this issue was to reduce the dose compared to the amount that could be administered based on clinical goals and animal weight. This strategy has been proposed elsewhere,[44] based on the argument that a reduced dose of a high molecular weight compound administered via a route that generates high bioavailability is likely to reduce skin irritation while maintaining therapeutic efficacy. Furthermore, the nature of the microneedle-mediated administration, wherein the drug is channeled directly into the dermis, has been shown to prevent drug-related skin irritation.[5] Indeed, no skin discoloration, swelling, or erythema was observed during and after the microneedle application. The piercing marks left on the skin postapplication, similar to the ones that have been observed in previous studies,[30] disappeared 5 min after removal (Figure 6f). Thus, the skin irritation study was not considered to be a requirement in the framework of the present study. In addition, piercing was done by applying very low forces to avoid animal discomfort due to the excellent piercing capacity of the μNe3dle arrays.

The plasma Dmab concentration was measured for each animal group, and the recorded data are shown in Figure 4g. The pharmacokinetic parameters are displayed in Table 2. The relative bioavailability (RBA) of the drug was calculated based on the following equation:

$$\%\mathrm{RBA} = \frac{\mathrm{AUC}_{\mathrm{3DMN}} \times \mathrm{dose}_{\mathrm{sc}}}{\mathrm{AUC}_{\mathrm{sc}} \times \mathrm{dose}_{\mathrm{3DMN}}} \quad (1)$$

Table 2. Pharmacokinetic Parameters of Dmab Administration

	pharmacokinetic parameters			
	C_{max} (ng/mL)	t_{min} (h)	AUC0−6 h	RBA (%)
untreated	0	0	0	0
SC	296.91 ± 15.3	1	1037.5	100
3DMN	245.5 ± 9.9	2	1038.1	100.06

A major limitation associated with delivery via subcutaneous injection is caused by back pressure produced during injection, which can delay the drug distribution and absorption. The use of hollow μNe3dles can act as a measure to tackle this issue in the sense that ejection from multiple openings can favor the broad and swift distribution of liquid within the skin tissue.

The plasma Dmab concentrations for the 6 h duration of the study are presented in Figure 4g and the respective pharmacokinetic parameters are displayed in Table 2. The data suggest that Dmab delivered by the 3D printed hollow μNe3dles produces similar rapid development of plasma concentrations compared to the administration with subcutaneous injection. The peak plasma concentration detected in the 3DMN group was found to be slightly lower than the SC; however, the %RBA values demonstrate that the two administration routes achieve almost equivalent results with no significant differences in pharmacokinetics. This is an important finding since the pharmacokinetic profile plays a significant role in bone formation and bone remodeling. The hourly measured concentrations of Dmab were further analyzed to obtain the secondary data on which the statistical data analysis was done. The null hypothesis for this study was that there is no significant difference between the data obtained from the SC and 3DMN groups while the alternate hypothesis was that there

https://doi.org/10.1021/acs.molpharmaceut.4c00379
Mol. Pharmaceutics 2024, 21, 4465−4475

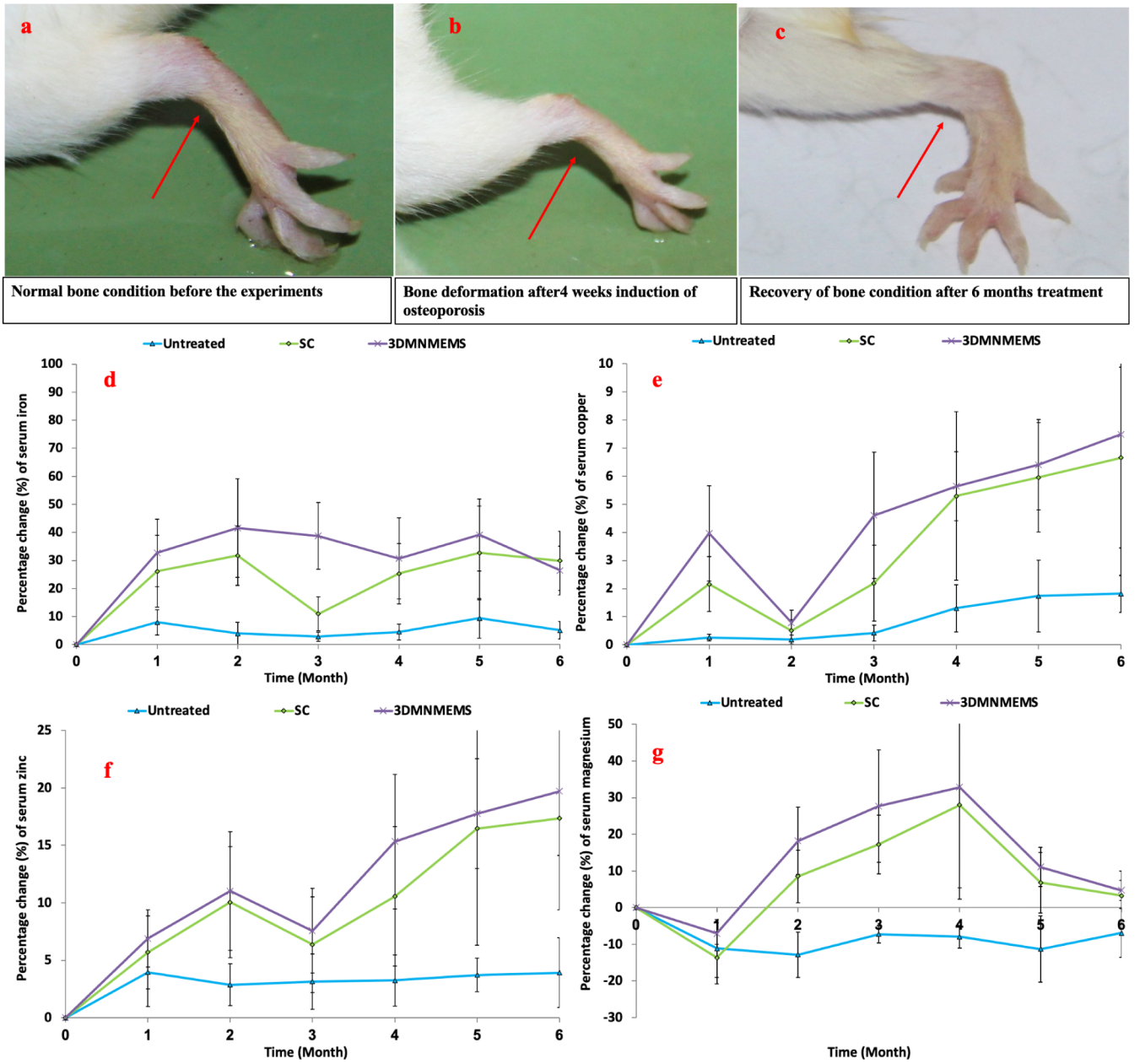

Figure 7. In vivo monitoring of bone mineral changes after Dmab administration to osteoporotic animals using subcutaneous injections and 3D printed hollow μNe3dles. (a) Healthy bone before ovariectomy; (b) deformed bone 4 weeks after ovariectomy; at this point, the animals are considered osteoporotic; (c) bone recovery at 6 months after animals received treatment; and monthly percentage change of serum (d) iron, (e) copper, (f) magnesium, and (g) zinc concentrations during the 6-month study.

is a significant difference between the data obtained from the SC and the 3DMN groups. *t* tests were carried out to compare the data from both animal groups, and small mean value differences were observed. The *p* value obtained from the *t* test was 0.4912, which means that the null hypothesis is accepted and there is no significant difference between the means of the two groups. This finding suggests that 3D printed hollow μNe3dles presented similar clinical efficacy to traditional subcutaneous injection routes for the in vivo administration of Dmab.

3.5. Quantification of Changes in Serum Bone Minerals. To evaluate the therapeutic effect of Dmab delivered by the 3D printed hollow μNe3dles, the quantification of changes in bone related minerals after confirmation of osteoporosis and Dmab administration was essential. A six-month study was conducted, wherein the serum concentrations of 4 different ions, namely, iron, magnesium, zinc, and copper, were recorded for the 3 animal groups studied (untreated, SC, and 3DMN, $n = 6$). The time interval between recordings was set at 1 month, and the data were collected at the same date of every month. Figure 7a–c illustrates the visually observable bone alterations attributed to the induction of osteoporosis in comparison to the healthy state, followed by evident recovery 6 months after the administration of Dmab.

Serum iron concentration data showed that the mineral gradually increased for the 3DMN animal group, with decreases being recorded at 4 and 6 months. The respective data of the SC group showed a similar but subtler increasing trend up until the third month when a significant decrease was observed. Overall,

https://doi.org/10.1021/acs.molpharmaceut.4c00379
Mol. Pharmaceutics 2024, 21, 4465−4475

the recovery of serum iron is evidently higher for the μNe3Dle treated animals for the whole duration of the study, indicating that the subcutaneously injected Dmab did not maintain stable state of serum iron. On the other hand, the trend of serum copper concentration followed similar patterns for both treated animal groups. The copper concentration showed a gradual increase with time, with an abrupt decrease at 2 months (Figure 7e) for both animal groups.

However, at all time points, the copper serum concentration for the animal group treated with hollow μNe3dles was found to be higher than the respective SC group. Along the same lines, the concentration of serum magnesium showed a similar gradual increase for the two groups, with the peak concentration recorded at 4 months post treatment. The Dmab fails to maintain high magnesium concentrations after that time point, as evinced by the decrease at months 5 and 6. This effect, however, appears to be irrelevant to the administration route. Finally, serum zinc concentration showed a similar increasing pattern for both animal groups, with a decrease at the third month of the study, which again seems to be independent of the administration route and pertinent to the pharmaceutical activity of the drug. In Figure 7d−g, a decrease of mineral concentration was observed in early months, since the animals went through surgical ovariectomy, and a single dose administration was injected at the beginning of the treatment. It was also attributed to the longer circulatory time of Dmab in the blood. Initially, the Dmab solution was injected underneath the skin and formed a depot in the dermal area, which was absorbed from the dermis to the blood by passive diffusion. The amounts of the studied bone minerals were measured before Dmab administration (Table 3) as well as after the conclusion of the 6-month monitoring period (Table 4).

Table 3. Baseline Amounts of Serum Bone Minerals Before the Treatment

	amount of serum iron (μg/dL)	amount of serum copper (μg/dL)	amount of serum magnesium (μg/dL)	amount of serum zinc (μg/dL)
untreated	32.3 ± 5.0	79.6 ± 7.0	2.4 ± 0.3	29.2 ± 2.3
SC	34.8 ± 2.5	86.8 ± 2.5	2.3 ± 0.5	30.9 ± 3.3
μNe3dles	28.9 ± 3.7	81.2 ± 4.6	2.2 ± 0.3	30.7 ± 1.3

Table 4. Amounts of Serum Bone Minerals 6 Months After Treatment

	amount of serum iron (μg/dL)	amount of serum copper (μg/dL)	amount of serum magnesium (μg/dL)	amount of serum zinc (μg/dL)
untreated	44.5 ± 5.1	84.2 ± 7.2	1.3 ± 0.2	35.8 ± 2.3
SC injection	135.6 ± 7.7	108.4 ± 4.6	3.4 ± 0.2	57.3 ± 5.4
μNe3dles	167.9 ± 7.6	107.2 ± 2.3	4.6 ± 0.7	63.6 ± 5.1

Statistical analysis on the percentage change of ion concentrations was performed to evaluate the significance of the SC and 3DMN data sets. Paired *t* test and ANOVA were used, and the confidence interval was set at 95%. Hence, for $p < 0.05$, the difference between bone mineral data obtained from the SC and 3DMN groups was considered statistically significant.

The *p* values obtained from the respective tests conducted on the iron, copper, magnesium, zinc, and copper data were 0.047, 0.0449, 0.00178, and 0.013, respectively (Table 5). In all 4 *t* tests, the value of *p* was less than 0.05, which verifies that there is a statistically significant difference between the bone mineral recovery in the SC injection and the 3DMN treated animals. To further validate this finding, ANOVA tests were performed. The respective *p* values calculated for iron, copper, magnesium, and zinc were 0.00147, 0.0379, 0.0101, and 0.026, which are all lower than the 0.05 threshold (Table 5). Summarizing, statistical analyses verify the hypothesis that the use of 3D printed hollow μNe3dles for Dmab delivery increases the serum concentration of the ions under investigation at a greater rate compared to the SC injection.

Table 5. Statistical Analysis for Bone Mineral Recovery Data Obtained for Animals Treated with SC Injection and 3D Printed Hollow μNe3dles

	changes of serum iron	changes of serum copper	changes of serum magnesium	changes of serum zinc
t test	0.047	0.0449	0.00178	0.013
ANOVA	0.00147	0.0379	0.0101	0.026

The data of this study generate an interesting finding. Although the relative bioavailability of the drug postadministration was almost identical for both administration routes, the therapeutic effect of Dmab delivered via hollow μNe3dles was superior in terms of bone mineral regain. At the end of the 6-month study, the majority of the studied bone-related minerals were found to be at higher amounts for the μNe3dle-treated animals compared to the injection treated ones. The explanation behind this effect may be associated with the long-term pharmacokinetics of the drug administered via the two different routes; however, additional research that is beyond the scope of the present article is required. In a similar study conducted by Courtenay et al. (2018), it was found that microneedle patches increased the in vivo bioavailability of bevacizumab, an antibody for cancer treatment.[8] Ding et al. (2023) introduced hydrogen peroxide-responsive microneedle patches for the delivery of delivery of integrin $\alpha_v\beta_6$-blocking antibody, which demonstrated excellent biocompatibility combined with specific targeting to lesions.[44] Nevertheless, our study demonstrated that in the future, 3D printed μNe3dles can be an alternative approach for delivering Dmab in humans. This could easily be done by coupling printed arrays in a pen-injector to control the administrated dose.

4. CONCLUSIONS

In this work, we presented a multifunctional platform device for drug administration based on hollow μNe3dles manufactured via 3D printing. The SLA 3D printing technology was employed to successfully fabricate complex hollow μNe3Dle arrays comprising a low-cost biobased resin with excellent printability (accuracy), mechanical properties, and skin permeability. The μNe3Dles were found to be equally as effective in administering Dmab to osteoporotic mice in comparison with subcutaneous injections. Although the bioavailability of the drug administered via the two approaches was similar, its therapeutic effect in terms of bone mineral restoration was superior for the μNe3dle-treated animals, as demonstrated after a 6-month study. Overall, this study puts forward the broader use of hollow μNe3dles as a more efficient alternative to typical needles. More importantly, the use of biobased materials paves the way for the development of biodegradable or recyclable medical devices and the adoption

https://doi.org/10.1021/acs.molpharmaceut.4c00379
Mol. Pharmaceutics 2024, 21, 4465−4475

of greener technologies. The use of 3D printing as the μNe3dle manufacturing technology further simplifies the development process of such intricate systems, thus increasing their attractiveness and enabling their fast and reliable production and subsequent use in the clinical setting.

AUTHOR INFORMATION

Corresponding Author

Dennis Douroumis − *Centre for Research Innovation, University of Greenwich, Medway Campus, Chatham Maritime, Kent ME4 4TB, United Kingdom;* orcid.org/0000-0002-3782-0091; Phone: +44 2083318440; Email: D.Douroumis@gre.ac.uk

Authors

Md Jasim Uddin − *Centre for Research Innovation, University of Greenwich, Medway Campus, Chatham Maritime, Kent ME4 4TB, United Kingdom; Department of Pharmaceutical Technology, Faculty of Pharmacy, Universiti Malaya, Kuala Lumpur 50603, Malaysia*

Sophia Nikoletta Economidou − *Medway School of Pharmacy, University of Kent, Medway Campus, Chatham, Kent ME4 4TB, United Kingdom*

Léa Guiraud − *École Nationale Supérieure de Chimie de Mulhouse, Université de Haute-Alsace, MULHOUSE Cedex 68 093, France*

Mohsin Kazi − *Kayyali Chair for Pharmaceutical Industries, Department of Pharmaceutics, College of Pharmacy, King Saud University, Riyadh 11451, the Kingdom of Saudi Arabia*

Fars K. Alanazi − *Kayyali Chair for Pharmaceutical Industries, Department of Pharmaceutics, College of Pharmacy, King Saud University, Riyadh 11451, the Kingdom of Saudi Arabia*

Complete contact information is available at: https://pubs.acs.org/10.1021/acs.molpharmaceut.4c00379

Notes

The authors declare no competing financial interest.

ACKNOWLEDGMENTS

The authors extend their appreciation to the Deanship of Scientific Research, King Saud University, for funding through Vice Deanship of Scientific Research Chairs; Research Chair of "Kayyali Chair for Pharmaceutical Industries".

REFERENCES

(1) Sozen, T.; Ozisik, L.; Calik Basaran, N. An overview and management of osteoporosis. *Eur. J. Rheumatol.* **2017**, *4* (1), 46−56.

(2) Moen, M. D.; Keam, S. J. Denosumab. *Drugs Aging.* **2011**, *28* (1), 63−82.

(3) Waghule, T.; Singhvi, G.; Dubey, S. K.; Pandey, M. M.; Gupta, G.; Singh, M.; Dua, K.; et al. Microneedles: A smart approach and increasing potential for transdermal drug delivery system. *Biomed. Pharmacother.* **2019**, *109* (October 2018), 1249−1258.

(4) Gill, H. S.; Denson, D. D.; Burris, B. A.; Prausnitz, M. R. Effect of microneedle design on pain in human subjects. *Clin J. Pain.* **2008**, *24* (7), 585−594.

(5) Katsumi, H.; et al. Efficient transdermal delivery of alendronate, a nitrogen-containing bisphosphonate, using tip-loaded self-dissolving microneedle arrays for the treatment of osteoporosis. *Pharmaceutics* **2017**, *9* (3), 29.

(6) Daddona, P. E.; Matriano, J. A.; Mandema, J.; Maa, Y. F. Parathyroid hormone (1−34)-coated microneedle patch system: Clinical pharmacokinetics and pharmacodynamics for treatment of osteoporosis. *Pharm. Res.* **2011**, *28* (1), 159−165.

(7) Tran, K. T. M.; et al. Single-Administration Long-Acting Microarray Patch with Ultrahigh Loading Capacity and Multiple Releases of Thermally Stable Antibodies, Mol. *Pharmaceutics* **2023**, *20* (5), 2352−2361.

(8) Courtenay, A. J.; McCrudden, M. T. C.; McAvoy, K. J.; McCarthy, H. O.; Donnelly, R. F. Microneedle-Mediated Transdermal Delivery of Bevacizumab, Mol. *Pharmaceutics* **2018**, *15* (8), 3545−3556.

(9) Andar, A. U.; Karan, R.; Pecher, W. T.; DasSarma, P.; Hedrich, W. D.; Stinchcomb, A. L.; DasSarma, S.; et al. Microneedle-Assisted Skin Permeation by Nontoxic Bioengineerable Gas Vesicle Nanoparticles, Mol. *Pharmaceutics* **2017**, *14* (3), 953−958.

(10) Guan, X.; Pei, Y.; Song, J. DNA-Based Nonviral Gene Therapy−Challenging but Promising, Mol. *Pharmaceutics* **2024**, *21* (2), 427−453.

(11) Shakya, A. K.; Lee, C. H.; Gill, H. S. Microneedle-mediated allergen-specific immunotherapy for the treatment of airway allergy in mice. *Mol. Pharmaceutics* **2020**, *17* (8), 3033−3042.

(12) Taha, E.; et al. Versatile Nanoparticulate Systems as a Prosperous Platform for Targeted Nose-Brain Drug Delivery, Mol. *Pharm.* **2024**, *21* (3), 999−1014.

(13) Taylor, L. S.; Amidon, G. L. Twenty Years of Molecular Pharmaceutics. *Mol. Pharm.* **2013**, *20* (12), 5947−5948.

(14) Donnelly, R.; Douroumis, D. Microneedles for drug and vaccine delivery and patient monitoring. *Drug Delivery And Transl. Res.* **2015**, *5* (4), 311−312.

(15) Al-Nimry, S. S.; Daghmash, R. M. Three dimensional printing and its applications focusing on microneedles for drug delivery. *Pharmaceutics* **2023**, *15* (6), 1597.

(16) Shim, D. H.; Nguyen, T. T.; Park, P.-G.; Kim, M. J.; Park, B.-W.; Jeong, H.-R.; Kim, D.-S.; Joo, H. W.; Choi, S.-O.; Park, J.-H.; Lee, J. M.; et al. Development of Botulinum Toxin A-coated microneedles for treating palmar hyperhidrosis. *Mol. Pharmaceutics* **2019**, *16* (12), 4913−4919.

(17) Mahfud, M. A. S.; Syahirah, N. A.; Akram, M.; Mahfufah, U.; Saputra, M. D.; Elim, D.; Andi, M. N. F.; Sultan, N. A. F.; Himawan, A.; Domínguez-Robles, J.; Pamornpathomkul, B.; et al. Solid dispersion incorporated into dissolving microneedles for improved antifungal activity of Amphotericin B: In vivo study in a fungal keratitis model. *Mol. Pharmaceutics* **2023**, *20* (12), 6246−6261.

(18) Tran, K. T. M.; Le, T. T.; Agrahari, V.; Peet, M. M.; Ouattara, L. A.; Anderson, S. M.; Le-Kim, T. H.; Singh, O. N.; Doncel, G. F.; Nguyen, T. D.; et al. Single-Administration Long-Acting Microarray Patch with Ultrahigh Loading Capacity and Multiple Releases of Thermally Stable Antibodies, Molecular Pharmaceutics 2023. *Mol. Pharmaceutics* **2023**, *20* (5), 2352−2361.

(19) Gaballa, S. A.; Shimizu, T.; Takata, H.; Ando, H.; Ibrahim, M.; Emam, S. E.; Amorim Matsuo, N. C.; Kim, Y.; Naguib, Y. W.; Mady, F. M.; Khaled, K. A.; et al. Impact of anti-PEG IgM induced via the topical application of a cosmetic product containing PEG derivatives on the antitumor effects of PEGylated liposomal antitumor drug formulations in mice. *Mol. Pharmaceutics* **2024**, *21* (2), 622−632.

(20) Tarbox, T. N.; Watts, A. B.; Cui, Z.; Williams, R. O. W., III An update on coating/manufacturing techniques of microneedles. *Drug Delivery Transl. Res.* **2018**, *8* (6), 1828−1843.

(21) Economidou, S. N.; Douroumis, D. 3D printing as a transformative tool for microneedle system: Recent advances, manufacturing considerations and market potential. *Adv. Drug Delivery Rev.* **2021**, *173*, 60−69.

(22) Pere, C. P. P.; et al. 3D printed microneedles for insulin skin delivery. *Int. J. Pharm.* **2018**, *544* (2), 425−432.

(23) Economidou, S. N.; et al. 3D printed microneedle patches using stereolithography (SLA) for intradermal insulin delivery. *Mater. Sci. Eng., C* **2019**, *102*, 743−755.

(24) Uddin, M. J.; Scoutaris, N.; Economidou, S. N.; Giraud, C.; Chowdhry, B. Z.; Donnelly, R. F.; Douroumis, D. 3D printed microneedles for anticancer therapy of skin tumours. *Mater. Sci. Eng., C* **2020**, *107* (October 2019), 110248.

(25) Voet, V. S. D.; Guit, J.; Loos, K. Sustainable photopolymers in 3D Printing: A review on biobased, biodegradable, and recyclable alternatives. *Macromol. Rapid Commun.* **2021**, *42* (3), 2000475.

(26) Zanoni, A.; Casiraghi, C.; Po, R.; Biagini, P.; Sponchioni, M.; Moscatelli, D.; et al. Redispersible Polymer Powders with High Bio-Based Content from Core−Shell Nanoparticles. *Macromol. Mater. Eng.* **2023**, *308* (1), 2200443.
(27) Klose, L.; Meyer-Heydecke, N.; Wongwattanarat, S.; Chow, J.; Pérez García, P.; Carré, C.; Streit, W.; Antranikian, G.; Romero, A. M.; Liese, A.; et al. Towards sustainable recycling of epoxy-based polymers: Approaches and challenges of epoxy biodegradation. *Polymers* **2023**, *15* (12), 2653.
(28) Voet, V. S. D.; Strating, T.; Schnelting, G. H. M.; Dijkstra, P.; Tietema, M.; Xu, J.; Woortman, A. J. J.; Loos, K.; Jager, J.; Folkersma, R.; et al. Biobased acrylate photocurable resin formulation for stereolithography 3D Printing. *ACS Omega* **2018**, *3* (2), 1403−1408.
(29) Teijido, R.; et al. Sustainable bio-based epoxy resins with tunable thermal and mechanic properties and superior anti-corrosion performance. *Polymers* **2023**, *15* (20), 4180.
(30) Economidou, S. N.; Uddin, J.; Marques, M. J.; Douroumis, D.; Sow, W. T.; Li, H.; Reid, A.; Windmill, J. F. C.; Podoleanu, A.; et al. A novel 3D printed hollow microneedle microelectromechanical system for controlled, personalized transdermal drug delivery. *Addit. Manuf.* **2021**, *38* (December 2020), 101815.
(31) Tabriz, A. G.; et al. Evaluation of 3D Printability and Biocompatibility of Microfluidic Resin for Fabrication of Solid Microneedles. *Micromachines* **2022**, *13* (9), 1368.
(32) Souza, V. R.; Mendes, E.; Casaro, M.; Antiorio, A. T. F. B.; Oliveira, F. A.; Ferreira, C. M. Description of Ovariectomy Protocol in Mice. In *re-Clinical Models: Techniques and Protocols. Methods in Molecular Biology, 1916P*; Humana Press: New York; 2019, 303309.
(33) Al-Nimry, S. S.; Daghmash, R. M. Three Dimensional Printing and Its Applications Focusing on Microneedles for Drug Delivery. *Pharmaceutics* **2023**, *15* (6), 1597.
(34) Voet, V. S. D.; Strating, T.; Schnelting, G. H. M.; Dijkstra, P.; Tietema, M.; Xu, J.; Woortman, A. J. J.; Loos, K.; Jager, J.; Folkersma, R. Biobased acrylate photocurable resin formulation for stereolithography 3D Printing. *ACS Omega* **2018**, *3* (2), 1403−1408.
(35) Prandato, E.; Livi, S.; Melas, M.; Auclair, J.; Verney, V.; Fleury, E.; Méchin, F.; et al. Effect of bio-based monomers on the scratch resistance of acrylate photopolymerizable coatings. *J. Polym. Sci., Part B: polym. Phys* **2015**, *53* (5), 379−388.
(36) Zeggai, N.; Bouberka, Z.; Dubois, F.; Bedjaoui, L.; Bouchaour, T.; Gherdaoui, C. E.; Potier, J.; Supiot, P.; Maschke, U.; et al. Tuning of thermally-induced shape memory properties of low-cost biocompatible linear and chemically crosslinked isobornyl/isobutylacrylate copolymers. *Compos. Sci. Technol.* **2022**, *219*, 109213.
(37) Böcherer, D.; Li, Y.; Kluck, S.; Nekoonam, N.; Zhu, P.; Rapp, B. E.; Kotz-Helmer, F.; Helmer, D. COLOR3D − Multicolored 3D printing of wood composites by submicron structuring. *Addit. Manuf.* **2023**, *75*, 103723.
(38) Economidou, S.; Pissinato Pere, C.; Okereke, M.; Douroumis, D. Optimisation of Design and Manufacturing Parameters of 3D Printed Solid Microneedles for Improved Strength, Sharpness, and Drug Delivery. *Micromachines* **2021**, *12* (2), 117.
(39) Uddin, M. J.; Scoutaris, N.; Klepetsanis, P.; Chowdhry, B.; Prausnitz, M. R.; Douroumis, D. Inkjet printing of transdermal microneedles for the delivery of anticancer agents. *Int. J. Pharm.* **2015**, *494* (2), 593−602.
(40) Deeks, E. D. Denosumab: A Review in Postmenopausal Osteoporosis. *Drugs And Aging.* **2018**, *35* (2), 163−173.
(41) Kirkby, M.; Hutton, A. R.; Donnelly, R. F. Microneedle Mediated Transdermal Delivery of Protein, Peptide and Antibody Based Therapeutics: Current Status and Future Considerations. *Pharm. Res.* **2020**, *37* (6), 117.
(42) Zhi, D.; Yang, T.; O'Hagan, J.; Zhang, S.; Donnelly, R. F. C. Photothermal therapy. *J. Controlled Release* **2020**, *325*, 52−71.
(43) Mönkäre, J.; Nejadnik, M. R.; Baccouche, K.; Romeijn, S.; Jiskoot, W.; Bouwstra, J. A IgG-loaded hyaluronan-based dissolving microneedles for intradermal protein delivery J. of Controlled Release. *J. Controlled Release* **2015**, *218*, 53−62.
(44) Ding, H.; Cui, Y.; Yang, J.; Li, Y.; Zhang, H.; Ju, S.; Ren, X.; Ding, C.; Zhao, J.; et al. ROS-responsive microneedles loaded with integrin avβ6-blocking antibodies for the treatment of pulmonary fibrosis. *J. Controlled Release* **2023**, *360*, 365−375.

https://doi.org/10.1021/acs.molpharmaceut.4c00379
Mol. Pharmaceutics 2024, 21, 4465−4475